

PAPER

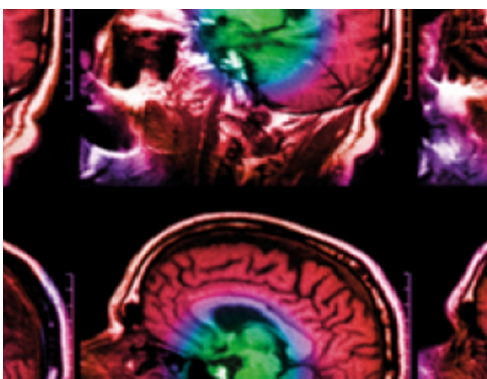
Elastometry of clot phantoms via magnetomotive ultrasound-based resonant acoustic spectroscopy

To cite this article: Benjamin E Levy and Amy L Oldenburg 2022 *Phys. Med. Biol.* **67** 155010

View the [article online](#) for updates and enhancements.

You may also like

- [Comparative study between electromagnet and permanent magnet rails for HTS maglev](#)
Yuyan Wen, Ying Xin, Wei Hong et al.
- [A deformation-based approach to tuning of magnetic micromechanical resonators](#)
Mahmut Bicer, Mohammad Nasr Esfahani, Arda D Yalcinkaya et al.
- [Imaging nanoparticle flow using magnetomotive optical Doppler tomography](#)
Jeehyun Kim, Junghwan Oh, Thomas E Milner et al.



IPEM | IOP

Series in Physics and Engineering in Medicine and Biology

Your publishing choice in medical physics,
biomedical engineering and related subjects.

Start exploring the collection—download the
first chapter of every title for free.



PAPER

Elastometry of clot phantoms via magnetomotive ultrasound-based resonant acoustic spectroscopy

Benjamin E Levy¹ and Amy L Oldenburg^{1,2} ¹ Department of Physics and Astronomy, The University of North Carolina at Chapel Hill, Chapel Hill, NC 27599, United States of America² Biomedical Research Imaging Center, The University of North Carolina at Chapel Hill, Chapel Hill, NC 27599, United States of AmericaE-mail: aold@physics.unc.edu**Keywords:** ultrasound, contrast-enhanced ultrasound, elastometry, magnetomotive ultrasound (MMUS)Supplementary material for this article is available [online](#)RECEIVED
21 March 2022REVISED
14 June 2022ACCEPTED FOR PUBLICATION
5 July 2022PUBLISHED
21 July 2022**Abstract**

Objective. An ultrasound-based system capable of both imaging thrombi against a dark field and performing quantitative elastometry could allow for fast and cost-effective thrombosis diagnosis, staging, and treatment monitoring. This study investigates a contrast-enhanced approach for measuring the Young's moduli of thrombus-mimicking phantoms. *Approach.* Magnetomotive ultrasound (MMUS) has shown promise for lending specific contrast to thrombi by applying a temporally modulated force to magnetic nanoparticle (MNP) contrast agents and measuring resulting tissue displacements. However, quantitative elastometry has not yet been demonstrated in MMUS, largely due to difficulties inherent in measuring applied magnetic forces and MNP densities. To avoid these issues, in this work magnetomotive resonant acoustic spectroscopy (MRAS) is demonstrated for the first time in ultrasound. *Main results.* The resonance frequencies of gelatin thrombus-mimicking phantoms are shown to agree within one standard deviation with finite element simulations over a range of phantom sizes and Young's moduli with less than 16% error. Then, in a proof-of-concept study, the Young's moduli of three phantoms are measured using MRAS and are shown to agree with independent compression testing results. *Significance.* The MRAS results were sufficiently precise to differentiate between thrombus phantoms with clinically relevant Young's moduli. These findings demonstrate that MRAS has potential for thrombus staging.

1. Introduction

From cancer to liver fibrosis, elastography plays a vital role in diagnosing a wide range of diseases, tracking their progression, and assessing their treatment (Szabo 2014, Ozturk *et al* 2018). An important example is deep vein thrombosis (DVT) where clot stiffness is clinically relevant for staging and treatment monitoring (Browse *et al* 1999, Symons Ettore and Lewis 2011). Quantitative ultrasound elastometry—the measure of elasticity, often in terms of Young's modulus—may rapidly inform DVT treatment decisions by providing a classification of the thrombus as acute or chronic. Current methods of ultrasound clot elastometry are in development (Bosio *et al* 2021), but not yet standardized, and could benefit from a contrast-enhanced technique due to the low echogenicity of many thrombi. Originally developed from optical coherence tomography (OCT) (Oldenburg *et al* 2005), and recently investigated for its ability to label thrombi (Pope *et al* 2013, Levy *et al* 2018), magnetomotive ultrasound (MMUS) is an emerging imaging modality in which magnetic nanoparticles (MNPs) are used as a contrast agent (Oh *et al* 2006, Sjöstrand *et al* 2020). MMUS has shown promise for elastometry applications due to its ability to remotely apply a magnetic force to the labeled region, and to measure the resulting displacement. Qualitative MMUS elastography was first presented in 2014 (Bruno *et al* 2014). It was later demonstrated that magnetically-induced motion in thrombus-mimicking phantoms decreased with Young's modulus (Levy *et al* 2018), and that displacement could be quantitatively predicted from Young's modulus in a simple, one-particle case (Levy and Oldenburg 2021). Toward the goal of quantitative elastometry

for thrombosis, in this work ultrasound magnetomotive resonant acoustic spectroscopy (MRAS) is used to measure the resonance frequencies and subsequently to quantify the Young's moduli of magnetically labeled thrombus phantoms.

In recent years, MMUS has been shown to have potential for elastometry, but challenges remain in quantifying the applied force. Elastometry is commonly performed by measuring the displacement resulting from a known force to calculate stress and strain. The ability to perform phase-resolved motion tracking with MMUS enables measuring displacements as small as tens of nanometers (Levy *et al* 2018), but determining the force requires knowledge of the magnetic properties and spatial distributions of MNPs in the imaging area. This is not possible with ultrasound, because MNPs are weak, sub-resolution acoustic scatterers. In 2019, Thapa worked to circumvent this issue by using an inverse model to reconstruct body force maps from MMUS displacement images up to a scaling factor (Thapa *et al* 2019). This factor could be determined under the assumptions of elastically homogeneous tissue and MNPs that are monodisperse in size and magnetic properties, but such assumptions may be limiting. More recently, Fink demonstrated a comparable technique that relies on finite element analysis (FEA) rather than an inverse model, but would require similar assumptions (Fink *et al* 2021). Taking another approach, Sjöstrand presented an echogenic MNP-labeled microbubble contrast agent that may allow for both quantification via ultrasound and displacement sensing via MMUS (Sjöstrand 2019). However, measurements in this study were made via laser vibrometry, and questions remain around how this would translate to MMUS, and whether the large microbubbles would be effective at labeling tissue. A different alternative comes from the analogous phase-resolved optical modality, magnetomotive optical coherence elastography. A temporally-sinusoidal magnetic force was applied and the shear wave velocity dispersion was measured in order to determine phantom Young's moduli (Ahmad *et al* 2014). Although this obviated the need for quantitative force measurements, it required the assumption of homogeneous mechanical properties, which would likely be violated near blood vessels. Ideally, MMUS elastometry would not have to rely on known forces or elastic homogeneity over a large area.

Resonant acoustic spectroscopy provides an exciting alternative for characterizing the mechanical properties of soft tissues, since increased vibration amplitude at resonance promises a higher signal-to-noise ratio without relying on quantitative force measurements (Oldenburg and Boppart 2010). Because this method depends on the geometry and boundary conditions of resonating structures being well known, it is ideal for measuring the Young's moduli of blood clots formed in microwells, which can be actuated via magnetic bead force transducers (Wu *et al* 2013, Krebs *et al* 2015). When using MNPs as transducers instead, the Young's moduli of gelatin phantoms have been demonstrated to affect their resonance frequencies (Oldenburg and Boppart 2010, Ersepke *et al* 2017), and with associated modelling based on phantom geometry, quantitative elastometry was shown to be possible with OCT (Oldenburg and Boppart 2010). To alleviate constraints due to the low penetration depth of light in tissue, in this work, MRAS is demonstrated for the first time using ultrasound. The resonance frequencies of MNP-labeled cylindrical gelatin thrombus phantoms are measured and shown to agree with simulated results generated via FEA. Then, resonance frequencies measured via MRAS are input into the finite element model, along with phantom dimensions measured via B-mode ultrasound, resulting in the first proof-of-concept FEA-based quantitative MMUS elastometry system.

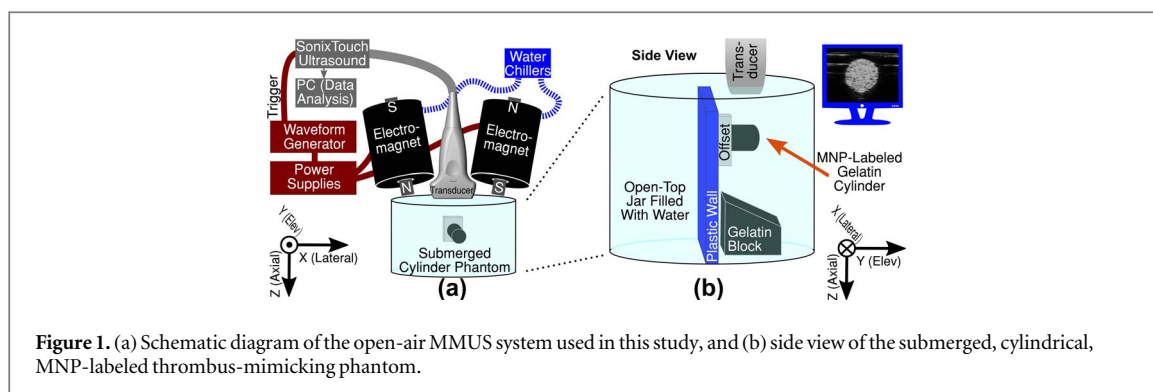
2. Methods

2.1. Open-air magnetomotive ultrasound apparatus

The MMUS system used in this work is shown in figure 1(a), and has been described previously (Levy *et al* 2018, Levy and Oldenburg 2021). Briefly, an Ultrasonix SonixTouch platform and an L14-5/38 transducer (Analogic Corporation, Peabody, MA, USA) were used for imaging. Antiparallel, water-cooled solenoid electromagnets were placed on either side of the transducer and were each driven by a Kepco ATE-75-15M, 1000 W power supply (Kepco Inc, Flushing, NY, USA). This configuration with the magnets flanking the transducer allowed for the imaging of large samples while maintaining a sufficient magnetic gradient of $\sim 0.02 \text{ T}^2/\text{m}$ in the imaging area. The power supplies were signaled by an Agilent 33522A arbitrary waveform generator (Keysight Technologies, Santa Rosa, CA, USA). B-mode images used to measure the phantom sizes were collected as per section 2.4.1, while MRAS data were collected as per section 2.4.2.

2.2. Gelatin thrombus-mimicking phantoms

The phantoms used for this study were designed to mimic the acoustic, geometric, and elastic characteristics of thrombi while being simple to create and simulate. As shown in figure 1(b), phantoms were gelatin cylinders approximately 4.5 mm in radius, and between 4 and 15 mm in length. Acoustic properties approximated those of human tissue with an attenuation of $0.3 \text{ dB cm}^{-1} \text{ MHz}^{-1}$ and 1540 m s^{-1} speed of sound. Because thrombi frequently resemble a structure fixed to a blood vessel wall on one side and otherwise surrounded by blood, the



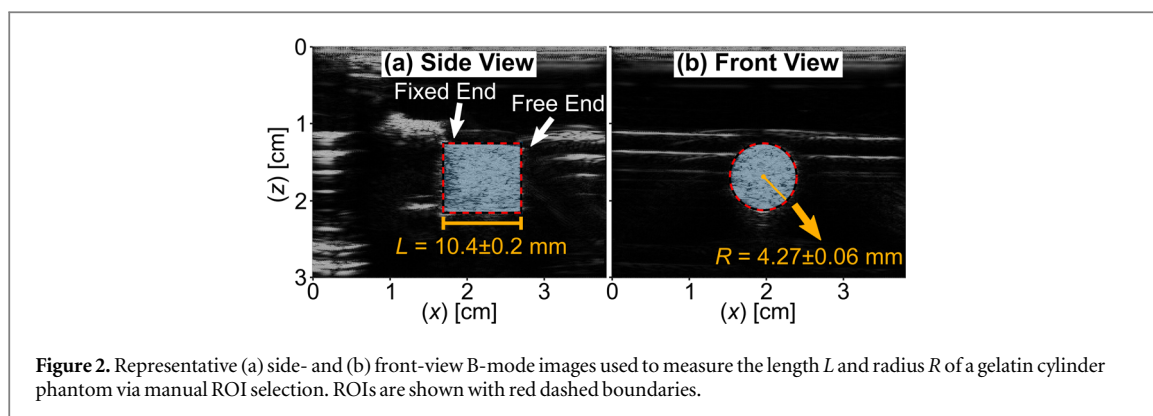
phantoms were fixed on one end to a plastic wall and submerged in an open-top jar of water. Young's moduli ranged from approximately 3–20 kPa by adjusting the gelatin concentration, which represents a clinically relevant range for thrombi. For example, a human study demonstrated that DVTs stiffen from ~ 2 to ~ 13 kPa as they age over two weeks (Liu *et al* 2017), and another found that DVTs maintain values at or below 7 kPa when subjects were given anticoagulants (Bosio *et al* 2021). Beyond DVT, abdominal aortic aneurysms have been shown to exhibit Young's moduli in the 13–60 kPa (Hinnen *et al* 2007) and 11–22 kPa (Ashton *et al* 2009) ranges. The phantoms were also labeled with MNPs for magnetomotive contrast.

Twelve magnetically labeled cylinders with a variety of lengths and Young's moduli were created for this study. The gelatin was prepared in 1.5 ml batches following a method similar to that originally described by Madsen (Madsen *et al* 1978) and Hall (Hall *et al* 1997). First, 1.25 ml of SHP-10 10 nm carboxyl coated iron oxide nanoparticle solution (Ocean NanoTech, San Diego, CA, USA) was added to a centrifuge tube for a final iron concentration of 4.2 mg Fe/ml. Gelatin from porcine skin (300 bloom, type A) was then added in different amounts to create 10 soft cylinders (3.2 wt%), 1 intermediate cylinder (4.5 wt%), and 1 stiff cylinder (8.7 wt%). The remainder of the volume was composed of synthetic graphite nanopowder (4.4 wt%), 1-propanol (3.0 wt%), and water. The solution was heated in a water bath to 50 °C with frequent vortexing, cooled to 28 °C, and then poured into a cylindrical phantom mold described in supplement I (available online at stacks.iop.org/PMB/67/155010/mmedia) for overnight gelation. The next day, the cylinders were removed from the mold and trimmed to the desired length. For the 10 soft cylinders, effort was made to produce an evenly spaced range of lengths between 4 and 16 mm, although trimming proved an imprecise process due to the floppy nature of the gelatin. The intermediate and stiff cylinders were fabricated with approximately the same lengths as three of the soft cylinders (10–11 mm).

Shortly after trimming, five-minute epoxy was used to fix one end of the cylinder to a small plastic 'offset,' which was, in turn, glued to the plastic vertical wall centered in the open-top jar. As shown in figure 1(b), this offset allowed the transducer to be positioned directly over the cylinder without touching the wall. After two hours, the jar was filled with room temperature tap water and a large, angled gelatin block with 4.4 wt% graphite nanopowder and 7.0 wt% gelatin was placed below the cylinder to reduce the severity of reflection artifacts. The jar was then situated in the imaging apparatus as shown in figure 1(b). Submerged phantoms were allowed to thermally equilibrate for 20 min before imaging because measurements were found to produce variable results until after this time.

2.3. Independent validation of young's modulus

In order to produce ground-truth Young's modulus values against which the MRAS system could be compared, compression tests were performed with a TA.XT Plus texture analyzer (Texture Technologies Corp., Hamilton, MA, USA). Three large (~ 100 ml) gelatin cylinders were created with the same ingredient concentrations as the soft, intermediate, and stiff phantoms, except that the nanoparticle solution was replaced with water. Then, the compression testing procedure utilized previously (Levy and Oldenburg 2021) was followed with two key differences. First, the cylinders were submerged in water during the compression tests, and second, rather than embedding thermocouples and monitoring Young's moduli as a function of temperature, the cylinders were simply allowed to thermally equilibrate in water for one hour before measurements. This longer equilibration period was necessary before results became consistent, likely due to the larger volume of these cylinders compared to the thrombus phantoms. Young's moduli were found to be 3.2 ± 0.2 , 7.6 ± 0.4 , and 20 ± 1 kPa for the soft, intermediate, and stiff cylinders, respectively, using the linear regions of the true stress–strain curves. Uncertainties were estimated from fit quality (R^2), and ambiguity of the linear region. It is interesting to note that while Hall's formula (Hall *et al* 1997) is usually accurate at predicting the Young's moduli for a given gelatin concentration, submersion of these phantoms caused a significant softening relative to samples measured in air.



2.4. Experimental data collection

For each cylinder, two different sets of data were collected. First, B-mode images with ultrasound parameters optimized for resolution were acquired for sizing the phantoms. Second, a stack of low-resolution images with parameters optimized for frame rate were collected for MRAS measurements.

2.4.1. Cylinder length and radius data collection

The ultrasound was set to collect one frame of RF data with an imaging depth of 3.0 cm, a width of 3.8 cm, and a 10 MHz transmit and receive frequency utilizing all 128 elements. The focal depth was set in each case to the center of the gelatin cylinder, usually ~ 1.5 cm. This produced an axial resolution of 0.08 mm, and a lateral resolution of ~ 0.2 mm. Two images were acquired immediately prior to MRAS data collection. In the first image, the transducer was oriented parallel to the cylinder axis to produce the ‘side view’ shown in figure 2(a). Then the transducer was rotated 90° into the position shown in figure 1 to produce the ‘front view’ in figure 2(b). The imaging plane was kept ~ 3 mm from the free end of the cylinder.

Beamformed RF data were imported into MATLAB R2020a (Mathworks Inc, Natick, MA, USA) on a separate PC, and manual region of interest (ROI) selection was used to extract the length and radius of each cylinder from the B-mode images. Example ROIs are shown with dashed red boundaries in figure 2. Uncertainties of ± 0.2 mm for length and ± 0.06 mm for radius were estimated. Although it was possible to extract radii from side view images, the uncertainty was found to be higher, so front view images were used for this purpose.

2.4.2. MRAS data collection

With the transducer still in the ‘front view’ position, the ultrasound settings were changed to an imaging depth of 2.5 cm and a width of 1.9 cm. Just 16 elements spaced evenly over the middle 50% of the array were used. This broadened the lateral resolution to ~ 0.9 mm, but allowed for a 532 Hz frame rate. For each cylinder, three stacks of beamformed RF data were collected while the magnets were driven with a square root-sinusoidal up-chirped current waveform. The result of this waveform was a 5 s sinusoidal up-chirped magnetic gradient force from 0 to 50 Hz acting on the embedded MNPs. The waveform was triggered by the start of data collection, and over 5 s of data were acquired for each image. The image stacks were then transferred to MATLAB for post-processing as discussed in section 2.7, where data beyond 5 s was omitted.

2.5. Finite element analysis

Gelatin cylinders with size, stiffness, material, and environmental parameters designed to match the experimental phantoms were simulated for FEA using COMSOL Multiphysics 5.6 (Comsol AB, Stockholm, Sweden).

2.5.1. Simulation parameters

In each simulated cylinder, the length, radius, and Young’s modulus were specified. The cylinder was oriented with its axis parallel to the ground, one end fixed, and the other free. A temporally chirped, spatially homogeneous 0–50 Hz sinusoidal body force was applied over the entire cylinder to approximate the experimental case where force amplitudes deviate less than 7% from the average over a typical phantom. The cylinders were also submerged in a 600 ml volume of water with an open top.

The *Solid Mechanics* module was used to model the motion of the cylinder as a linear elastic material with a semi-incompressible Poisson’s ratio of 0.495 and a density of 1000 kg m^{-3} , while the *Laminar Flow* module was used to model the motion of the water assuming incompressible flow and no turbulence. The *Fluid-Structure Interaction* multiphysics module was used to model the interfaces. A tetrahedral mesh was employed with

variable element volumes which averaged 1.4 mm^3 in the gelatin region, and 300 mm^3 in the water region. Mesh sizes were set via a mesh refinement study, and COMSOL automatically placed smaller elements close to interfaces and curved surfaces.

2.5.2. Data collection

Each FEA simulation consisted of a 5 s time dependent study using the 2nd-order backwards differentiation formula solver. Output times were set to $1/(532 \text{ Hz})$ to match the ultrasound sampling times, and solver step sizes were set to be less than or equal to $1/(532 \text{ Hz})$. For vibrating rods, three types of modes are possible: flexural (motion perpendicular to the rod's axis), extensional (motion parallel to the axis), and torsional (rotation about the axis) (Love 1944). Because the force was directed perpendicular to the cylinders' axes, the simulations exclusively excited flexural modes with motion parallel to the force. After each simulation, the volume-averaged displacement of the cylinder was output as a function of time. These data were then sent to MATLAB for determination of the resonance frequency (see section 2.7). FEA was chosen due to the lack of a straightforward analytical solution for this problem, but there is an analytical solution in the case that the cylinder is surrounded by air rather than water (Oldenburg and Boppart 2010). In this case analytical predictions matched simulations, lending further credibility to the FEA results.

2.5.3. Uncertainty analysis

Uncertainty in FEA resonance frequency results arose from underlying input parameter uncertainties. For each simulated cylinder of length L , radius R , and Young's modulus E with respective uncertainties σ_L , σ_R , and σ_E , two additional simulations were run to determine the upper and lower bounds. Shorter, wider, and stiffer cylinders exhibited higher resonance frequencies, so for the upper bound simulation, length was minimized ($L - \sigma_L$), while radius was maximized ($R + \sigma_R$), and Young's modulus was maximized ($E + \sigma_E$). Conversely, the lower bound was created by maximizing L while minimizing R and E . Gray-shaded uncertainty ranges in result figures were obtained from sweeps of multiple upper and lower-bound simulations across the plotted independent variable range. Cubic spline interpolation was used to form the edges.

2.6. MRAS measurement principle

Following the procedure suggested by Lathi and Green (2018), and previously employed by Oldenburg (Oldenburg and Boppart 2010) and Krebs (Krebs *et al* 2015), the resonance frequency f_0 of a simulated or experimental cylinder is determined by fitting a Lorentzian to its complex, frequency-domain transfer function, or 'mechanical spectral response.' Briefly, the MRAS system applies a chirped, sinusoidal magnetic driving force $F(t)$, and measures the resulting volume-averaged displacement $\Delta z(t)$. The mechanical spectral response is determined by considering the response of the system to a complex analytic harmonic driving force $\tilde{F}(t) = \tilde{F}e^{i\omega t}$ of angular frequency ω . The cylinder is then approximated as a driven, damped harmonic oscillator with complex analytic displacement $\Delta\tilde{z}$ such that

$$\Delta\tilde{z}''(t) + \gamma_0\Delta\tilde{z}'(t) + \omega_0^2\Delta\tilde{z}(t) \propto \tilde{F}(t), \quad (1)$$

where γ_0 and $\omega_0 = 2\pi f_0$ are the damping coefficient and fundamental resonance frequency, respectively. The solution to this differential equation is then

$$\Delta\tilde{z}(t) = \tilde{A}e^{i\omega t}, \quad (2)$$

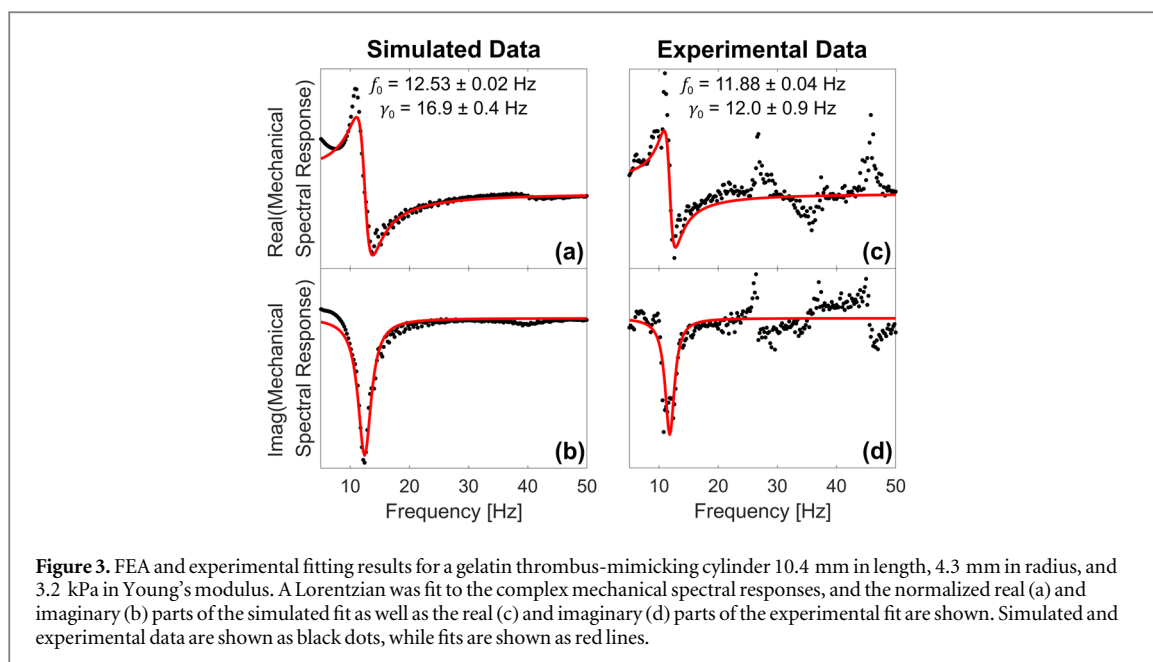
where \tilde{A} is

$$\tilde{A} = \tilde{I}\tilde{F} \propto \frac{\tilde{F}}{\omega_0^2 - \omega^2 + i\omega\gamma_0}, \quad (3)$$

such that the mechanical spectral response \tilde{I} is a complex Lorentzian that depends upon the driving frequency ω . The magnitudes of \tilde{A} and \tilde{F} represent the displacement and force amplitudes, respectively, while the phases of \tilde{A} and \tilde{F} represent the phase offsets of the displacement and force waveforms, respectively. For an arbitrary force $F(t)$ such as the chirped MRAS waveform, a Fourier decomposition produces a sum of phasors with amplitudes $\tilde{F}(\omega) = \mathcal{F}\{F(t)\}$. Given the linearity of differential equation (1), the resulting complex displacement amplitudes are thus $\tilde{A}(\omega) = \mathcal{F}\{\Delta z(t)\} = \tilde{I}(\omega)\tilde{F}(\omega)$ such that the mechanical spectral response is the ratio of the Fourier-transformed displacement and force (Lathi and Green 2018)

$$\tilde{I}(\omega) = \frac{\mathcal{F}\{\Delta z(t)\}}{\mathcal{F}\{F(t)\}} \propto \frac{1}{\omega_0^2 - \omega^2 + i\gamma_0\omega}. \quad (4)$$

Thus, experimental and simulated data are fit to a complex Lorentzian of the form given in (4) to extract the resonance frequency f_0 . Technical details are given in section 2.7.



2.7. MRAS data processing protocol

A similar procedure was used to determine the resonance frequencies of each experimental and simulated thrombus-mimicking cylinder, but the method of preparing data for analysis was different. In the experimental case, beamformed RF data were processed per the procedure outlined in Pope (Pope *et al* 2013). A Hilbert transform was applied to the stack of images, and the complex acoustic phase was subtracted pixel-wise from successive time samples to create a new stack of differential phase images. Differential phase is proportional to displacement and is less affected by low-frequency noise. The images were cropped to the boundaries of the cylinder, and pixels with intensities below 60% of the average B-mode intensity were rejected to minimize phase noise. For simulations, FEA data arrived from COMSOL ready to analyze as a one-dimensional vector of volume-averaged displacements sampled in time.

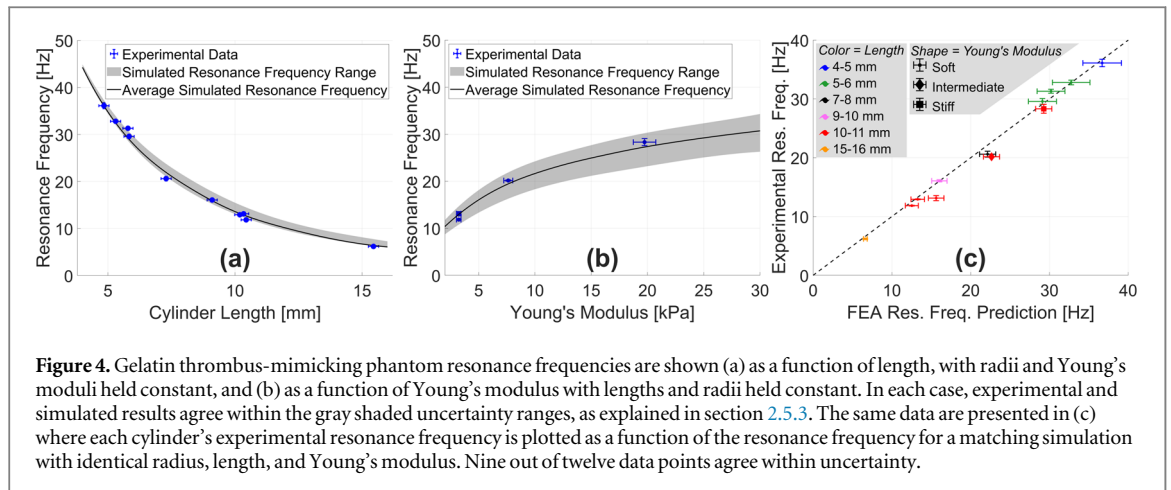
For both types of data, a Fourier transform was applied in time and divided elementwise by the Fourier transform of the corresponding chirped force waveform to create the mechanical spectral response according to (4). The ideal chirped waveform from the simulations was used for the FEA data, while the square of the current waveform measured directly from one of the magnets was used in the experimental case. The simulated data were already one-dimensional, but the experimental data were not, so after computing the Fourier transform of each pixel, a phasor average over the spatial dimensions was computed in the latter case. A nonlinear least-squares curve fitter was applied to the real and imaginary parts of the mechanical spectral responses as shown in figure 3. This was an improvement over a previously reported amplitude and phase fitting procedure (Oldenburg and Boppart 2010, Krebs *et al* 2015), as it avoided phase wrapping and minimized the residual across both bases simultaneously. For readers more familiar with amplitude and phase plots, supplement II contains the absolute value and argument of these same data and complex fits. The final resonance frequency for each experimental cylinder was determined by averaging the results of the three image stacks collected, and standard uncertainty was calculated by combining in quadrature uncertainty in the fit parameters with the standard deviation of these repeated measurements. Simulation uncertainties are discussed in section 2.5.3.

It should be noted that multiple higher frequency modes are visible in the experimental data in figure 3, but not in the simulated data. These are attributed to extensional or torsional modes of vibration. As discussed in section 2.5.2, higher frequency modes were not excited in the simulations, but might be excited in the experiments due to small magnetic force components perpendicular to the imaging plane. With appropriate analysis, such modes may present an additional means of measuring cylinder sizes and stiffnesses, but in general this would necessitate the ability to measure frequencies above 50 Hz. Thus, a maximum frequency was manually selected for these fits to exclude the higher modes when present.

3. Results

3.1. Experimental MRAS results agree with FEA

The blue dots in figure 4(a) show experimental thrombus-mimicking phantom resonance frequencies measured via MRAS as a function of length for all ten 'soft' cylinders. Each sample had a Young's modulus of



3.2 ± 0.2 kPa as measured by compression testing, and approximately constant radii of 4.4 ± 0.4 mm. The black line indicates the FEA predicted resonance frequencies for cylinders ranging from 4 to 16 mm in length, and the gray region represents the uncertainty in FEA results as described in section 2.5.3. All experimental resonance frequencies match FEA predictions within uncertainty.

Similarly, the blue dots in figure 4(b) show experimental phantom resonance frequencies measured via MRAS as a function of Young's modulus for five cylinders of similar size. Each sample had lengths and radii of 10.3 ± 0.1 mm and 4.8 ± 0.5 mm, respectively. Young's modulus values were measured via compression testing. The black line indicates the FEA predicted resonance frequencies for cylinders ranging from 3 to 30 kPa in stiffness, and the gray shaded region represents the uncertainty in the FEA results as described in section 2.5.3. Once again, all experimental resonance frequencies match FEA predictions within uncertainty. Note that the three nearly overlapping data points in the bottom left-hand corner are shared between this plot and figure 4(a).

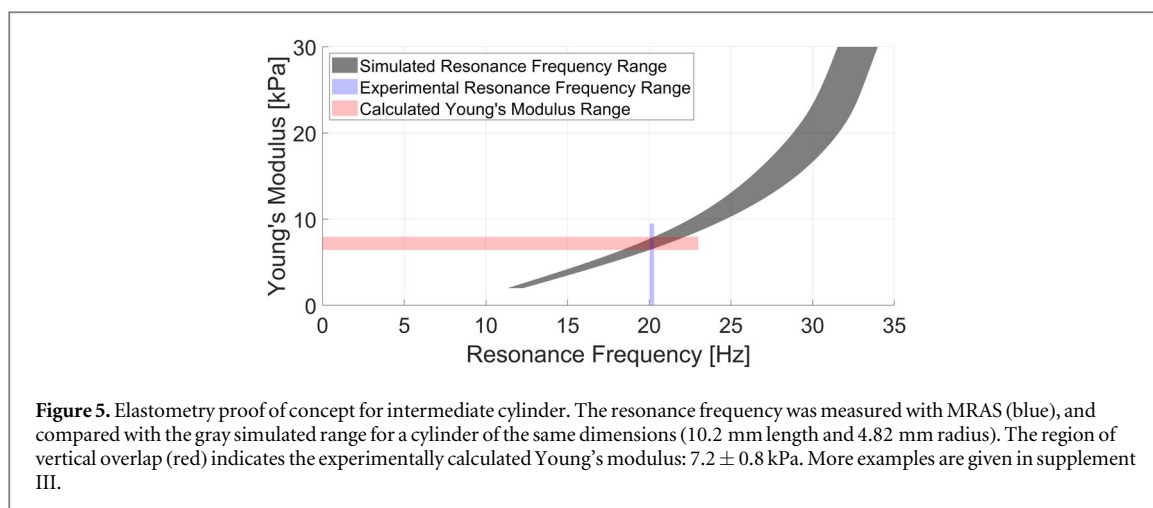
The data points in figure 4(c) represent the experimental resonance frequencies determined with MRAS for all twelve cylinders plotted as a function of the FEA predicted resonance frequencies. Simulated cylinders with the same lengths, radii, and Young's moduli were used in each case. Each color represents a range of cylinder lengths, while each marker shape represents a Young's modulus. Ideally, each point would lie on the dashed ' $y = x$ ' line. Nine of the data points agree within one standard deviation, while all twelve have $<16\%$ error. The fact that three results agree with simulations in figures 4(a) and (b), but not in figure 4(c) is due to the different FEA input parameters. For example, in figure 4(b) simulations used average experimental L and R values, which led to higher uncertainty than in figure 4(c) where results were compared against matched simulations.

3.2. Proof-of-concept elastometry results

In order to demonstrate the potential utility of ultrasound-based MRAS for measuring Young's moduli, the resonance frequency, length, and radii of three cylinders were determined from ultrasound data only, as acquired in section 2.4. An example plot of the elastometry process is given in figure 5, and full results are in supplement III. For each cylinder, a set of simulations with dimensions set via B-mode ultrasound measurements and Young's moduli ranging from 3 to 30 kPa were performed. The gray region in figure 5 represents the uncertainty bounds for this range of simulations, and was computed per the procedure in section 2.5.3. The blue region represents the experimentally observed resonance frequency range within one standard deviation, and the vertical area of overlap between the blue and gray regions represents the Young's moduli consistent with the observed resonance range. Thus, for the intermediate cylinder, the Young's modulus determined via MRAS was 7.2 ± 0.8 kPa, indicated by the red shaded area. This agrees with the independent compression testing result of 7.6 ± 0.4 kPa. Plots for the soft and stiff cylinders are given in supplement III. The soft cylinder was found to have $E = 3.5 \pm 0.4$ kPa, while the stiff cylinder was found to have $E = 18 \pm 4$ kPa, both of which agree with the compression testing results (3.2 ± 0.2 and 20 ± 1 kPa, respectively) and are mutually distinguishable.

4. Discussion

The resonance frequencies of twelve cylindrical gelatin thrombus-mimicking phantoms were measured via MRAS and compared to simulated results from FEA. Experimental data agreed with FEA predictions when cylinder lengths were varied (figure 4(a)), and when cylinder Young's moduli were varied (figure 4(b)). Additionally, the Young's moduli of three phantoms with different gelatin concentrations were measured using



a combination of B-mode ultrasound and MRAS. The results for the soft, intermediate, and stiff cylinders were 3.5 ± 0.4 , 7.2 ± 0.8 , and 18 ± 4 kPa, respectively, and plots further demonstrating the process used to arrive at these results are presented in supplement III. Each measurement agreed with Young's moduli measured via independent compression tests, and exhibited uncertainty ranges small enough to allow for differentiation between the three stiffnesses. Specifically, the percent error in each case was between 10 and 25, which may be sufficient to distinguish acute from chronic thrombi. For example, in a study of DVT in mice, acute thrombi initially exhibited Young's moduli of ~ 2 kPa before stiffening to ~ 13 kPa over the course of two weeks (Liu *et al* 2017)—an increase of 550%. Such measurements were possible despite the different dimensions of the three cylinders, which raises the possibility of a future blinded study to establish whether this method has prognostic value for positively identifying “soft” phantoms from amongst those with a range of stiffnesses. The goal would be to mirror the need for efficient differentiation between acute and chronic thrombi in the clinic (Browse *et al* 1999, Symons Ettore and Lewis 2011).

In this work, a simple gelatin cylinder fixed at one end and submerged in water was used as a thrombus-mimicking phantom for experimental and FEA simplicity. However, because this model does not perfectly recapitulate the geometry and environment of a thrombus *in vivo*, certain limitations arise. First, real thrombi are not generally cylindrical, and they may be smaller than the phantoms used in this study. This could lead to higher resonance frequencies with lower displacement amplitudes, while the magnets used in this work were not optimized for supplying forces at frequencies above 50 Hz. This is not a fundamental limitation, and higher frequency modulation may be achieved through an improved magnetic force delivery system (Ersepke *et al* 2017, Wang *et al* 2019). Additionally, in an *in vivo* situation, there usually exists echogenic tissue between the transducer and the blood vessel, but in this work that space was filled only with water. Furthermore, this distance is often substantial, with DVT potentially occurring deep inside the leg. A study of 2816 people in the 1980s found an average thigh radius of 8.8 cm, with a 95th percentile of 11 cm (Heitmann and Frederiksen 2009), which approximates the maximum necessary imaging depth. While to date MMUS systems have been designed for depths up to 5 cm (Pope *et al* 2013), further improvements in magnetic delivery may be needed to ensure adequate force and sufficiently low attenuation and clutter to allow for MRAS in less favorable conditions. Finally, pulsatile blood flow may be confounding in the cases of arterial thrombi or venous thrombi in the vicinity of arterial motion; although previous work has demonstrated MMUS imaging in the presence of physiological flow at a fixed magnet modulation frequency (Levy *et al* 2018), additional strategies may be needed to extract a chirped waveform under these conditions. Because blood flow also imparts shear stress on the thrombus, it may need to be accounted for in future FEA models along with the mechanical properties of the blood and vessel walls.

Although the specifics of labeling thrombi were not the focus of this study, the feasibility of achieving sufficient MNP concentrations for MRAS is important, and warrants further investigation. Previous work has demonstrated that platelets, a primary constituent of thrombi, may be labeled with an average of 140 fg Fe of super-paramagnetic iron oxide nanoparticles per platelet (Pope *et al* 2013). Progress has been made toward using magnetically labeled platelets to visualize thrombi via magnetomotive OCT (Oldenburg *et al* 2010, 2012) and ultrasound (Pope *et al* 2013). In the former case, rehydrated, lyophilized platelets were loaded with MNPs, and pumped through *ex vivo* porcine arteries with and without damage to the luminal wall. Magnetomotive OCT imaging provided specific contrast to the damaged regions (Oldenburg *et al* 2010), but so far this has not been realized *in vivo*. Besides labeling platelets themselves, the use of receptors that mediate platelet aggregation and adhesion as targets for magnetic contrast warrant further study. For example, the interaction between

glycoprotein (GP) Ib- α and von Willebrand factor (VWF) is crucial for thrombus formation, while the binding of VWF to both GPIIb/IIIa and collagen mediate thrombus growth (Jamasbi *et al* 2017). Magnetic contrast agents capable of targeting such receptors may provide another method for specific labeling of thrombi. Regardless of the contrast mechanism, it is worth considering whether non-uniform labeling could alter resonance frequencies. The results of a preliminary study detailed in supplement IV showed qualitatively consistent results for two cylinders of similar size where one was labeled uniformly with MNPs, and the other was labeled non-uniformly with a single 1-mm-diameter magnetic ball. Additionally, resonance frequencies did not change as a function of position within the uniformly labeled phantoms.

Lastly, a model with a wider geometric parameter space could be used to account for the more general case of thrombi without cylindrical cross sections. The geometry of the thrombus, which is needed for input into the FEA model, could be obtained with the same MNPs via MMUS, which has shown promise for volume measurements (Levy *et al* 2018). Furthermore, simulations currently take approximately 45 min to run on a 3.3 GHz Intel Xeon quad-core E-2124 processor, and an Nvidia Quadro P620 graphics card. Enhanced hardware and software optimization could allow for a wider range of geometries, sizes, and boundary conditions to be simulated more quickly, perhaps on a per-measurement, on-demand basis.

Acknowledgments

B E Levy thanks D R T Sampaio with GIIMUS at the University of São Paulo at Ribeirão Preto for his patient and generous ultrasound technical support.

This work was supported in part by the National Institutes of Health under grant R21 HL 119928, and by the Department of Defense Air Force Office of Scientific Research under grant FA9550-14-1-0208.

ORCID iDs

Benjamin E Levy  <https://orcid.org/0000-0001-6806-3647>

Amy L Oldenburg  <https://orcid.org/0000-0002-2642-8350>

References

- Ahmad A, Kim J, Sobh N A, Shemonski N D and Boppart S A 2014 Magnetomotive optical coherence elastography using magnetic particles to induce mechanical waves *Biomed. Opt. Express* **5** 2349–61
- Ashton J H, Vande Geest J P, Simon B R and Haskett D G 2009 Compressive mechanical properties of the intraluminal thrombus in abdominal aortic aneurysms and fibrin-based thrombus mimics *J. Biomech.* **42** 197–201
- Bosio G, Zenati N, Destremes F, Chayer B, Pernod G and Cloutier G 2021 Shear Wave elastography and quantitative ultrasound as biomarkers to characterize deep vein thrombosis *in vivo* *J. Ultrasound Med.* **41** 1807–16
- Browse N L, Burnand K G, Irvine A T and Wilson N M 1999 Deep vein thrombosis: pathology *Diseases of The Veins* 2nd edn (London: Arnold) pp 249–89
- Bruno A C *et al* 2014 Magnetomotive ultrasound elastography: preliminary evaluation in phantom *Brazilian Congr. Biomed. Eng.* 6–9
- Ersepke T, Kranemann T C and Schmitz G 2017 Frequency response of soft tissue displacements induced by the force on magnetic nanoparticles *IEEE Int. Ultrasonics Symp., IUS (Washington, DC, 06–09 September 2017)* (Picastaway, NJ: IEEE) pp. 1–4
- Fink M, Rupitsch S J, Lyer S and Ermert H 2021 Quantitative determination of local density of iron oxide nanoparticles used for drug targeting employing inverse magnetomotive ultrasound *IEEE Trans. Ultrason. Ferroelectr. Freq. Control* **68** 2482–95
- Hall T J, Bilgen M, Insana M F and Krouskop T A 1997 Phantom materials for elastography *IEEE Trans. Ultrason. Ferroelectr. Freq. Control* **44** 1355–65
- Heitmann B L and Frederiksen P 2009 Thigh circumference and risk of heart disease and premature death: Prospective cohort study *Br. Med. J.* **339** b3292
- Hinnen J W, Rixen D J, Koning O H J, van Bockel J H and Hamming J F 2007 Development of fibrinous thrombus analogue for in vitro abdominal aortic aneurysm studies *J. Biomech.* **40** 289–95
- Jamasbi J, Ayabe K, Goto S, Nieswandt B, Peter K and Siess W 2017 Platelet receptors as therapeutic targets: past, present and future *Thromb. Haemost.* **117** 1249–57
- Krebs C R, Li L, Wolberg A S and Oldenburg A L 2015 A portable blood plasma clot micro-elastometry device based on resonant acoustic spectroscopy *Rev. Sci. Instrum.* **86** 1–11
- Lathi B P and Green R A 2018 Continuous-time system analysis using the laplace transform *Linear Systems and Signals* 3rd edn (New York: Oxford University Press) pp 330–487
- Levy B E, Hossain M M, Sierchio J M, Thapa D, Gallippi C M and Oldenburg A L 2018 Effect of model thrombus volume and elastic modulus on magnetomotive ultrasound signal under pulsatile flow *IEEE Trans. Ultrason. Ferroelectr. Freq. Control* **65** 1380–8
- Levy B E and Oldenburg A L 2021 Single magnetic particle motion in magnetomotive ultrasound: an analytical model and experimental validation *IEEE Trans. Ultrason. Ferroelectr. Freq. Control* **68** 2635–44
- Liu X, Li N and Wen C 2017 Effect of pathological heterogeneity on shear wave elasticity imaging in the staging of deep venous thrombosis *PLoS One* **12** 1–15
- Love A E H 1944 Vibrations of rods. problems of dynamical resistance *A treatise on the Mathematical Theory of Elasticity* 4th edn (New York: Dover) pp 427–43
- Madsen E L *et al* 1978 Tissue mimicking materials for ultrasound phantoms *Med. Phys.* **5** 391–4

- Oh J, Feldman M D, Kim J, Condit C, Emelianov S and Milner T E 2006 Detection of magnetic nanoparticles in tissue using magneto-motive ultrasound *Nanotechnology* **17** 4183–90
- Oldenburg A L *et al* 2010 Magnetic and contrast properties of labeled platelets for magnetomotive optical coherence tomography *Biophys. J.* **99** 2374–83
- Oldenburg A L and Boppart S A 2010 Resonant acoustic spectroscopy of soft tissues using embedded magnetomotive nanotransducers and optical coherence tomography *Phys. Med. Biol.* **55** 1189–201
- Oldenburg A L, Gunther J R and Boppart S A 2005 Imaging magnetically labeled cells with magnetomotive optical coherence tomography *Opt. Lett.* **30** 747–9
- Oldenburg A L, Wu G, Spivak D, Tsui F, Wolberg A S and Fischer T H 2012 Imaging and elastometry of blood clots using magnetomotive optical coherence tomography and labeled platelets *IEEE J. Sel. Top. Quantum Electron.* **18** 1100–9
- Ozturk A, Grajo J R, Dhyani M, Anthony B W and Samir A E 2018 Principles of ultrasound elastography *Abdom. Radiol.* **43** 773–85
- Pope A G *et al* 2013 Contrast-enhanced imaging of SPIO-labeled platelets using magnetomotive ultrasound *Phys. Med. Biol.* **58** 7277–90
- Sjöstrand S *et al* 2019 Contrast-enhanced magnetomotive ultrasound imaging (CE-MMUS) for colorectal cancer staging: assessment of sensitivity and resolution to detect alterations in tissue stiffness *IEEE Int. Ultrasonics Symp., IUS* **9–12**
- Sjöstrand S, Evertsson M and Jansson T 2020 Magnetomotive ultrasound imaging systems: basic principles and first applications *Ultrasound Med. Biol.* **46** 2636–50
- Symons Ettore A and Lewis B D 2011 The peripheral veins *Diagnostic Ultrasound* 4th edn, ed C M Rumack, S R Wilson, J W Charboneau and D Levine (Philadelphia: Elsevier) pp 1023–38
- Szabo T L 2014 Elastography *Diagnostic Ultrasound Imaging: Inside Out* 2nd edn (Oxford: Academic) pp 699–733
- Thapa D, Levy B E, Marks D L and Oldenburg A L 2019 Inversion of displacement fields to quantify the magnetic particle distribution in homogeneous elastic media from magnetomotive ultrasound *Phys. Med. Biol.* **64** 125019
- Wang H W, Huang C C and Li M L 2019 Improved backward mode pulsed magnetomotive ultrasound via pre-magnetization of superparamagnetic iron oxide nanoparticles *IEEE Int. Ultrason. Symp. IUS* **2019** 2387–9
- Wu G, Krebs C R, Lin F C, Wolberg A S and Oldenburg A L 2013 High sensitivity micro-elastometry: applications in blood coagulopathy *Ann. Biomed. Eng.* **41** 2120–9